Supplementary Information for

Self-Assembled Structures in Rod-Coil Block Copolymers with Hydrogen-Bonded Amphiphiles

Han-Sheng Sun[1], Chia-Hao Lee[1], Chia-Sheng Lai[3], Hsin-Lung Chen[3], Shih-Huang Tung[,1], and Wen-Chang Chen*[,1,2]*

*Corresponding authors. email: shtung@ntu.edu.tw; chenwc@ntu.edu.tw

1. GPC Measurements

The carrier solvents commonly used for GPC experiments are THF, DMF and chloroform. However, Poly(4-vinylpyridine) (P4VP) is insoluble in THF and may aggregate in chloroform while polyfluorene (PF) can't be dissolved in DMF. We thus have difficulty to find a proper solvent to conduct the GPC tests of PF-*b*-P4VP block copolymers. The only rational data we obtained were from PF_9-*b*-$P4VP_{22}$, which can be dissolved in DMF to high extent probably because the molecular weight is small so that the dilute mixture of PF_9-*b*-$P4VP_{22}$ in DMF can gain higher mixing entropy. For other block copolymers, we always found large aggregates and couldn't obtain useful data. The GPC chromatogram of PF_9-*b*-$P4VP_{22}$ is shown in Figure S1.

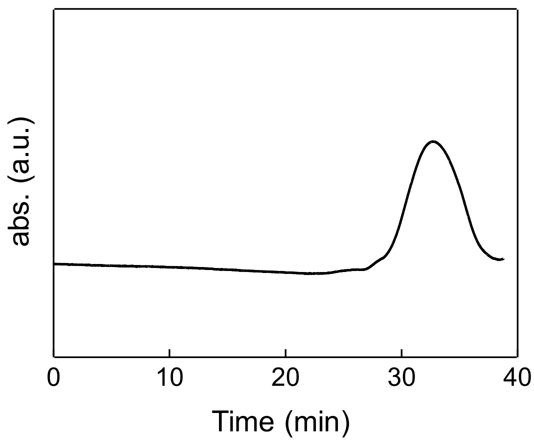

Figure S1. GPC data of PF_9-*b*-$P4VP_{22}$. The sample was dissolved in DMF. The PDI is estimated to be 1.78.

2. Morphology of Other PF-*b*-P4VPs

Other than the PF_9-based series of rod-coil block copolymers discussed in the paper, we have also synthesized and characterized copolymers with varying lengths of blocks, which are listed in Table S1. The degree of polymerization of the PF-vinyl macroinitiators are determined by ^{1}H NMR and confirmed by GPC. The PDIs from GPC are ~ 2.10 for PF_{17} and PF_{21}. The PDIs of the block copolymers are thus expected to be in the range between 1.20 and 2.10 (The PDIs of the P4VP homopolymers we synthesized were ~1.20). The TEM and AFM images of the block copolymers are shown in Figure S2-S4. It is found that the fraction of each block is the key in controlling the morphology and the copolymers with similar fraction show the same morphology.

Table S1. Characteristics of PF-*b*-P4VP rod-coil block copolymers

Sample	$M_{n,PF}$ [b]	$M_{n,P4VP}$ [b]	f_{4VP} [c]	T_g (°C)	Morphology	Figure
PF_{17}-*b*-$P4VP_{38}$ [a]	5960	3990	0.40	109	lamella	S2
PF_{17}-*b*-$P4VP_{233}$	5960	24460	0.80	147	sphere	S3
PF_{21}-*b*-$P4VP_{40}$	7060	4220	0.37	101,142	lamella	S4

[a] subscriptions denote degree of polymerization

[b] molecular weight determined by NMR

[c] weight fraction of P4VP

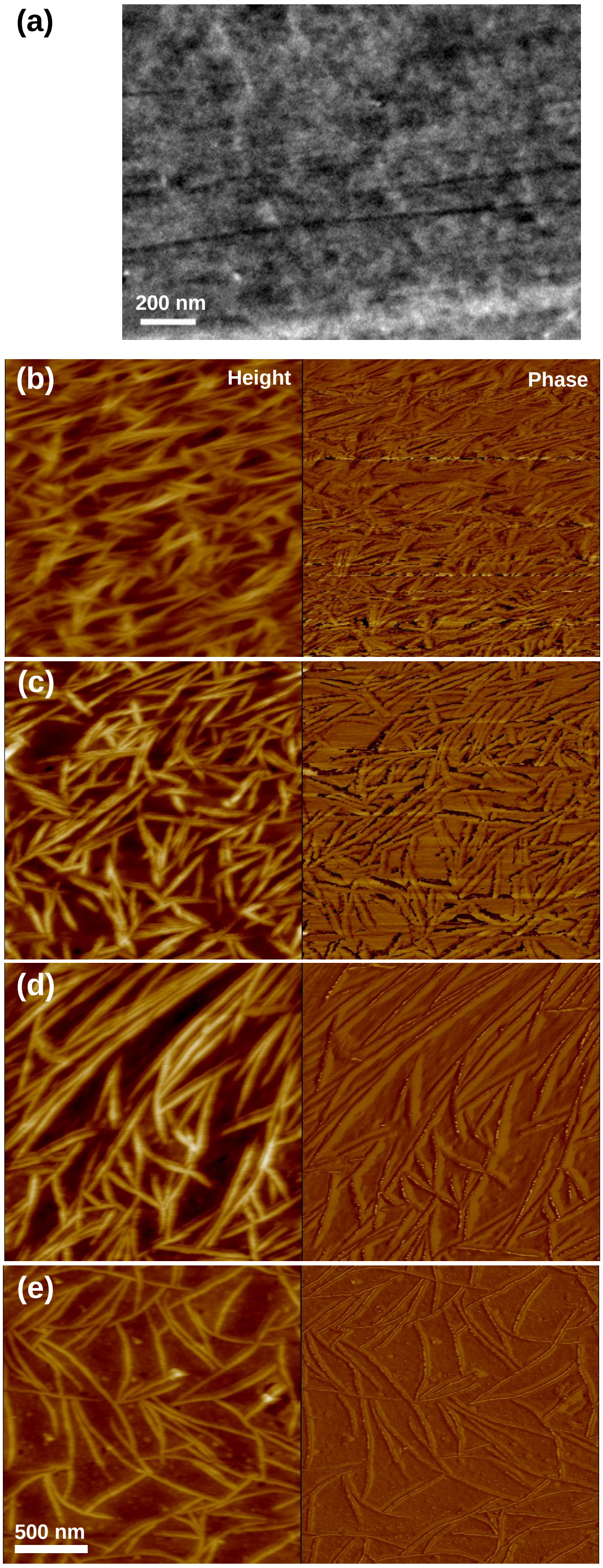

Figure S2. Structure characterization of PF_{17}-*b*-$P4VP_{38}$: (a) TEM image of a bulk sample. The TEM sample was stained with RuO_4. AFM images for thin films with thickness (b) 104 nm, (c) 46 nm, (d) 26 nm, and (e) 18 nm. The dependence of morphology on thickness is similar to that of PF_9-*b*-$P4VP_{22}$.

(a)

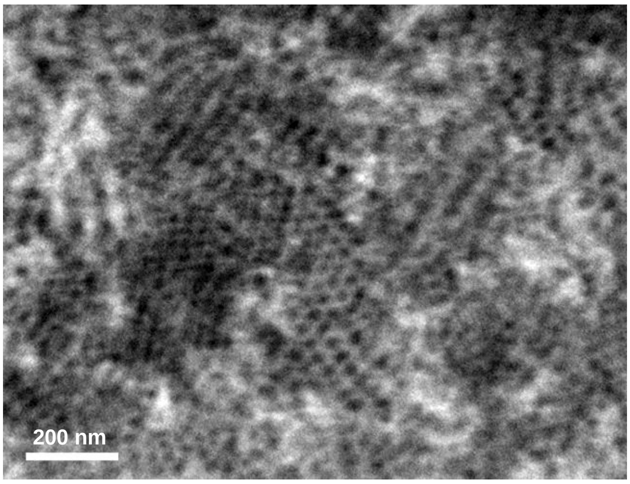

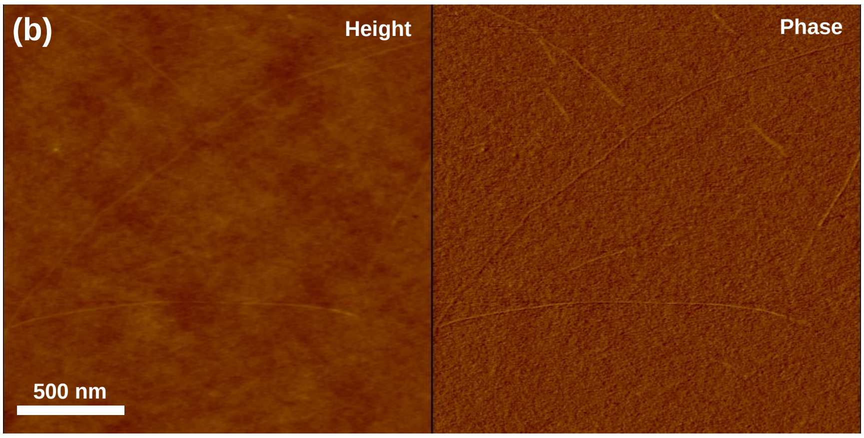

Figure S3. Structure characterization of PF_{17}-*b*-$P4VP_{233}$: (a) TEM image of a bulk sample, showing spherical PF microdomains. The TEM sample was stained with RuO_4. (b) AFM images of a thin film with thickness ~ 98 nm. Due the low contrast between PF and P4VP, the surface is basically smooth.

(a)

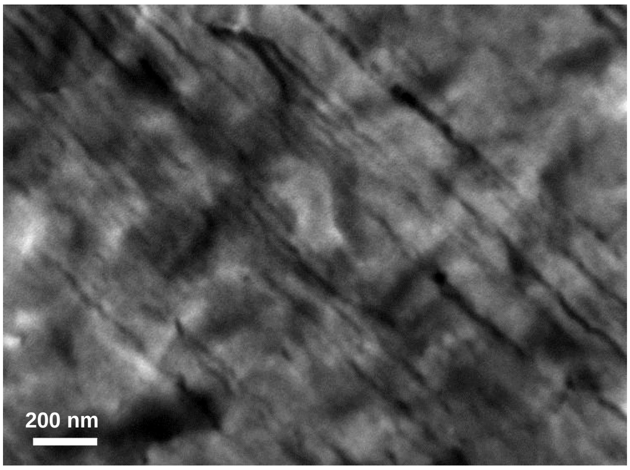

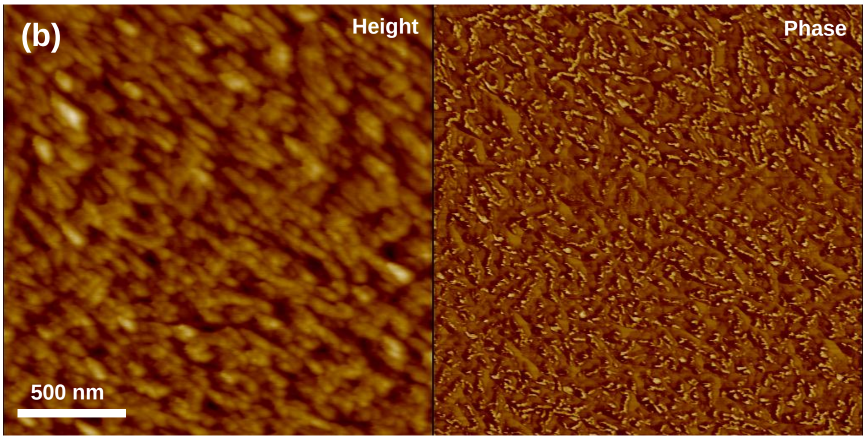

Figure S4. Structure characterization of PF_{21}-*b*-$P4VP_{40}$: (a) TEM image of a bulk sample. The TEM sample was stained with RuO_4. (b) AFM images for a thin film with thickness ~ 41 nm.

3. Morphology of Other PF-*b*-P4VP(PDP)s

Other complexes of PF-*b*-P4VP(PDP)$_x$ with different ratio of PDP to 4VP are listed in Table S2. The AFM images of each complex are shown in Figure S5 to S12. The complete phase diagram is illustrated in Figure 10 in the paper. It is clear that the addition of PDP alters the volume fraction of P4VP(PDP) and in turn, leads to a transition of morphology.

Table S2. Characteristics of PF-*b*-P4VP(PDP) supramolecules

Sample	f_{comb}[a]	Morphology	Figure
PF_9-*b*-$P4VP_{22}(PDP)_{0.5}$	0.64	cylinder	S5
PF_9-*b*-$P4VP_{92}(PDP)_{0.5}$	0.88	cylinder + sphere	S6
PF_{17}-*b*-$P4VP_{38}(PDP)_{0.3}$	0.56	lamella	S7
PF_{17}-*b*-$P4VP_{38}(PDP)_{0.5}$	0.62	lamella + cylinder	S8
PF_{17}-*b*-$P4VP_{38}(PDP)_{0.7}$	0.67	cylinder	S9
PF_{17}-*b*-$P4VP_{38}(PDP)_{1.0}$	0.72	cylinder	S10
PF_{17}-*b*-$P4VP_{233}(PDP)_{1.0}$	0.94	sphere	S11
PF_{21}-*b*-$P4VP_{40}(PDP)_{1.0}$	0.70	cylinder	S12

[a] weight fraction of P4VP(PDP)

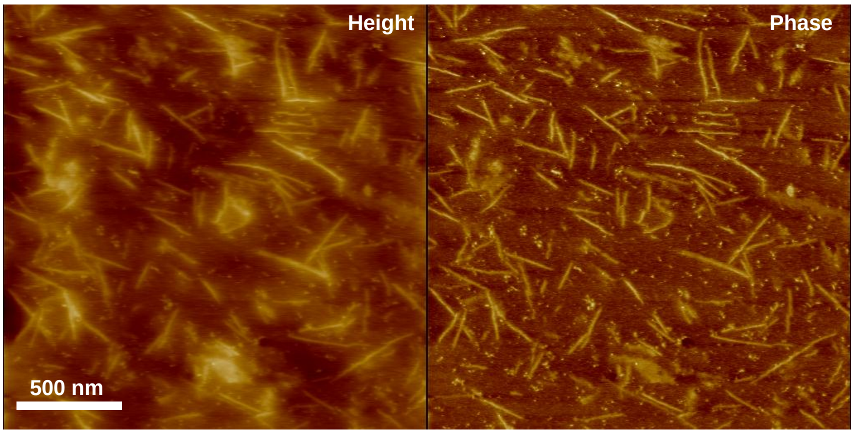

Figure S4. AFM images of a PF_9-*b*-$P4VP_{22}(PDP)_{0.5}$ thin film, thickness = 70 nm.

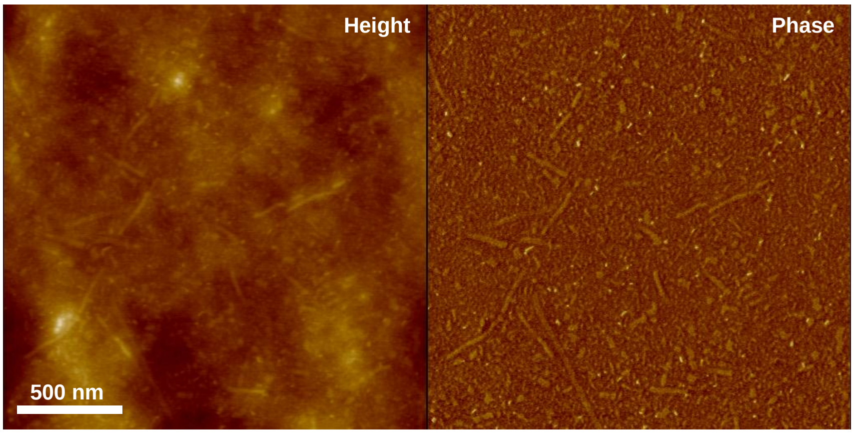

Figure S6. AFM images of a PF_9-*b*-$P4VP_{92}(PDP)_{0.5}$ thin film, thickness = 251 nm.

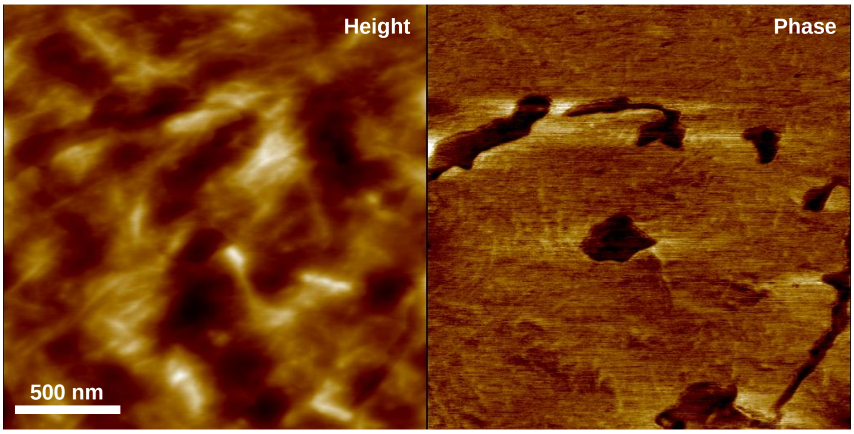

Figure S7. AFM images of a PF_{17}-*b*-$P4VP_{38}(PDP)_{0.3}$ thin film, thickness = 145 nm. The surface is featured with holes, which are characteristic of thin films with parallel lamellar microdomains.

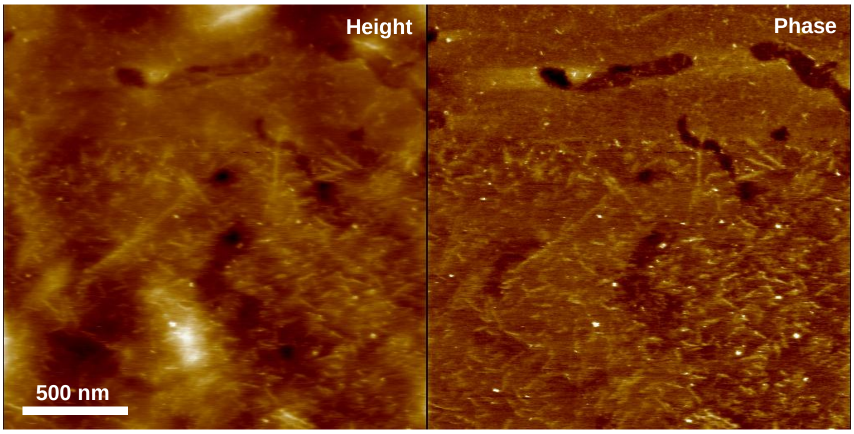

Figure S8. AFM images of a PF$_{17}$-*b*-P4VP$_{38}$(PDP)$_{0.5}$ thin film, thickness = 204 nm.

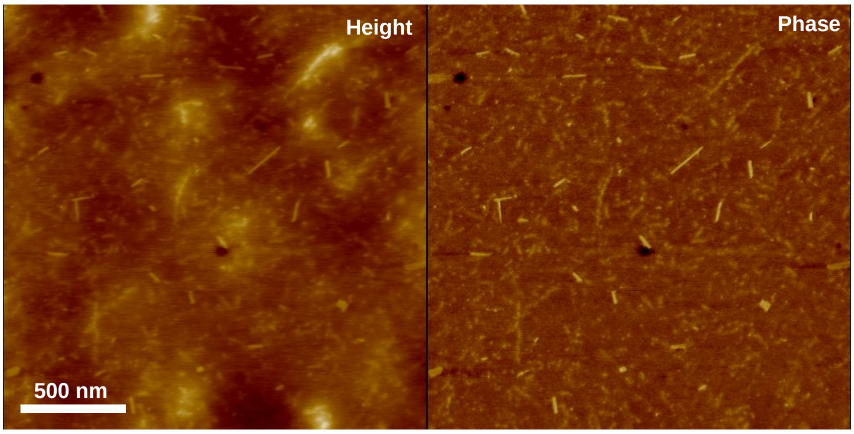

Figure S9. AFM images of a PF$_{17}$-*b*-P4VP$_{38}$(PDP)$_{0.7}$ thin film, thickness = 144 nm.

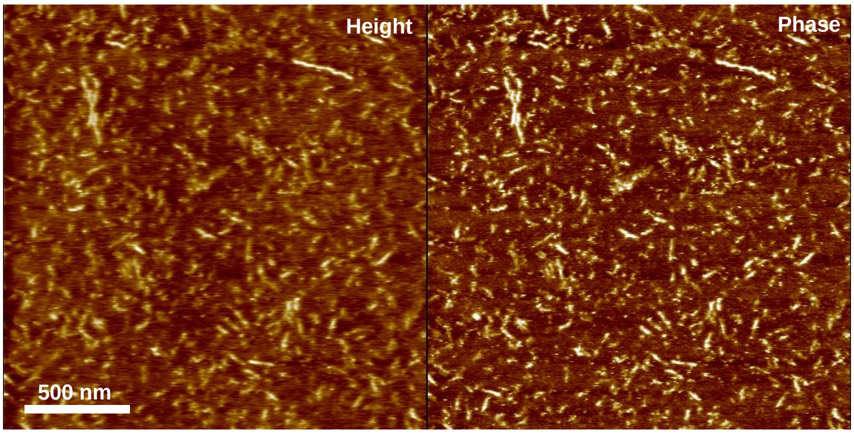

Figure S10. AFM images of a PF$_{17}$-*b*-P4VP$_{38}$(PDP)$_{1.0}$ thin film, thickness = 332 nm.

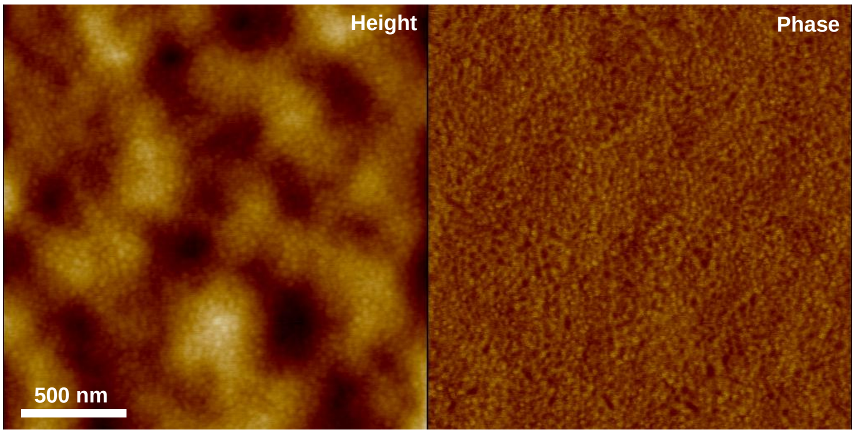

Figure S11. AFM images of a PF_{17}-*b*-$P4VP_{233}(PDP)_{1.0}$ thin film, thickness = 247 nm.

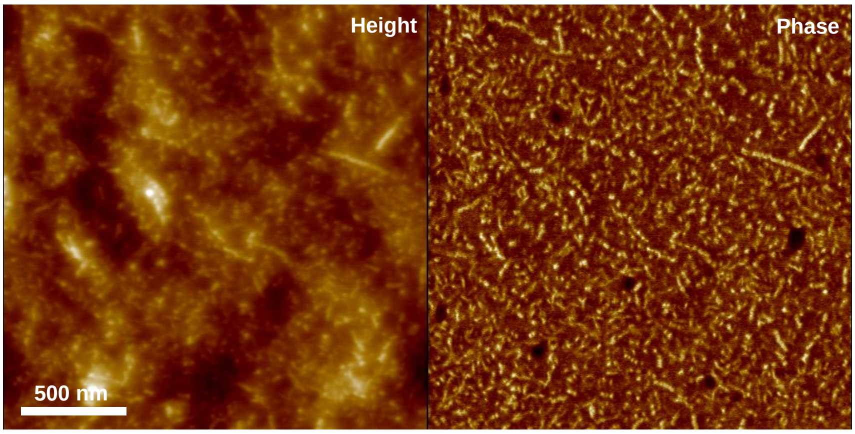

Figure S12. AFM images of a PF_{21}-*b*-$P4VP_{40}(PDP)_{1.0}$ thin film, thickness = 531 nm.